Oxygen K-edge X-ray absorption spectra of ThO_2 and CeO_2: Experiment, interpretation, and structural effects

Lucia Amidani, Thomas Dumas, David Shuh, Sergei Butorin, Christoph Sahle, Alessandro Longo, Kristina Kvashnina

Oxygen K-edge X-ray Absorption Spectra of ThO_2 and CeO_2: experiment, interpretation and structural effects.

Lucia Amidani,[1,2] Thomas Dumas,[3] David K. Shuh,[4] Sergei M. Butorin,[5] Christoph J. Sahle,[6] Alessandro Longo,[6] Kristina O. Kvashnina[1,2*]*

[1]The Rossendorf Beamline at ESRF – The European Synchrotron, 38043 Grenoble, France.

[2]Helmholtz-Zentrum Dresden-Rossendorf, Institute of Resource Ecology, 01328 Dresden, Germany.

[3]CEA, DES, ISEC, DMRC, Univ. Montpellier, 30207 Bagnols sur Cèze, France.

[4]Lawrance Berkeley National Laboratory, Berkeley, California 94720, USA.

[5] Condensed Matter Physics of Energy Materials, X-ray Photon Science, Department of Physics and Astronomy, Uppsala University, P.O. Box 516, SE-751 20 Uppsala, Sweden.

[6] ESRF, The European Synchrotron, 71 Avenue des Martyrs, CS40220, 38043 Grenoble Cedex 9, France.

KEYWORDS. Actinides, XANES, thorium dioxide.

ABSTRACT. Experimental oxygen K-edge spectra of ThO_2 and CeO_2 are presented and interpreted based on density functional theory (DFT). The contribution of *d* and *f* orbitals to the O K-edge spectrum are identified as well distinguished peaks, the presence of which evidences the strong hybridization of Th and Ce metal centers with O orbitals. The sensitivity of the O K-edge to both *f*- and *d*-states in the absence of a core-hole on the metal ion results in an insightful overview of the electronic structure involved in the chemical bond. In particular, the large bandwidth of the Th 5*f* band as compared to the Ce 4*f* band is observed as a set of wider and more substantial set of peaks in the O K-edge, confirming the stronger hybridization of the former with O orbitals. The peak ascribed to the 5*f* band of ThO_2 is found at higher energy than the 6*d* band, as predicted from DFT calculations on actinide dioxides. To highlight the sensitivity and the potential use of the O K-edge for the characterization of ThO_2-based systems, the sensitivity of the spectrum to structural changes such as lattice expansion and size reduction are calculated and discussed.

INTRODUCTION. Understanding the physico-chemical properties of actinide materials will foster progresses in several fields of science. The quest for advanced nuclear fuel, the safe disposal of nuclear waste, preventing environmental contamination by radionuclides and promoting new applications of actinide materials are goals that require understanding the fundamentals of these materials.[1] One inherent characteristic that makes actinides unique is the presence of the 5*f* orbitals in the set of valence orbitals.[2,3] From the accrued knowledge on actinides, we nowadays know that in the first half of the series, the 5*f* electrons participate to chemical bonding.[3–7] Determining and

quantifying the involvement of 5*f* and 6*d* orbitals in actinide chemical bonds is currently of great importance and interest,[7–18] in particular for the enormous impact a rigorous understanding of the chemical behavior of actinides could have on the field of separations chemistry. Few techniques can access this information and a prominent role is played by XANES. In recent years, XANES at the actinide $M_{4,5}$ edges[19–32] and at the ligand K-edge[11–14,33–39] has been largely used. While $M_{4,5}$ edges probe directly the 5*f* orbitals, the ligand K-edge is sensitive to actinide 5*f* and 6*d* orbitals only through their mixing with ligand *p* orbitals. XANES at the ligand K-edge involves transitions of a 1*s* core electron, strongly localized on the ligand, to an unoccupied state of the allowed symmetry. The presence at the K-edge of spectral features from the metal 5*f*/6*d* orbitals is only possible if these states are involved in the unoccupied states probed by the photoelectron and therefore it is a direct probe of orbital mixing.[40] Many ligand K-edges of interest are in the soft X-ray regime and routine XANES measurements requires ultra-high vacuum (UHV). This represents a difficult constraint for the safe manipulation of actinide materials and limits the access to soft X-ray XANES for actinide research to a few high performance locations. The use of non-resonant inelastic X-ray scattering (NIXS), which can access edges of a few tens to a few hundreds of eV using hard X-rays, is a convenient possibility for ligand K-edge measurements on actinide systems.[41–46] The similarity of K-edges in the soft X-rays measured with NIXS at low momentum transfer and XANES is well assessed[47,48] as also demonstrated by measurements at the O K-edge of CeO_2 presented in this work.

To extract information on the electronic structure from XANES at the ligand K-edge, a correct interpretation of the spectra is essential. DFT[11–14,37–39,49] and sophisticated quantum chemistry approaches[15] were successfully used to interpret the ligand K-edge XANES on actinide molecular systems and to quantify the mixing of 4*f* orbitals in lanthanide dioxides.[49,50] The projected density

of states (DOS) obtained with density functional theory (DFT) were used to identify the 5*f* contribution to the O K-edge XANES of bulk UO_2, NpO_2 and PuO_2[35,36]. Surprisingly, the O K-edge XANES of ThO_2 has never been the focus of accurate interpretation and is rarely encountered in literature.[51,52] This work fills this gap by reporting experimental O K-edge XANES of ThO_2 and its interpretation based on theoretical calculations. The results on ThO_2 are compared with the well-known case of CeO_2 and with literature data on light-actinide dioxides. To highlight the sensitivity of O K-edge XANES to structural changes, we theoretically investigate the effects on the spectra of lattice expansion and of size reduction. Our results i) confirm that the 5*f* band is higher than the 6*d* band in ThO_2, as predicted by DFT calculations,[53,54] ii) indicate that both 6*d* and 5*f* Th orbitals are strongly involved in bonds with O, iii) predict a high sensitivity of the O K-edge XANES to structural modifications.

METHODS.

SYNTHESIS AND MEASUREMENTS OF ThO_2. Thorium dioxide was synthesized using an oxalic conversion route. Thorium nitrate, $Th(NO_3)_4{\cdot}5H_2O$, was used as precursor. The oxalate precipitate was synthesized in a vortex reactor (V = 20 mL) under ambient conditions by mixing a solution of Th(IV) ([Th(IV)] = 0.135 M) and a concentrated $H_2C_2O_4$ solution (with a slight excess of oxalic acid [$H_2C_2O_4$] = 0.05 M) in nitric medium ([HNO_3] = 2 mol.L^{-1}).[55–57] The time of addition of the actinide solution and oxalic acid solution was fixed at 3 minutes. The resulting crystallized powders, $Th(C_2O_4)_2.6H_2O$, were filtered after 10 min of maturation and dried at room temperature. The oxide was formed by calcination under air. The temperature was raised at a rate of 5°C·min^{-1} up to 600°C and the sample was left one hour at the maximum temperature.

The O K-edge XANES of ThO_2 was acquired at the Molecular Environmental Science (MES) Beamline 11.0.2 of the Advanced Light Source (Lawrence Berkeley National Laboratory, USA) equipped with a scanning transmission X-ray microscope (STXM).[58] The available energy range was approximately 100–2000 eV and the energy resolution of the measurements was less than 0.1 eV at the O K-edge. For the STXM measurements, the ThO_2 powder was sandwiched between two Si_3N_4 windows and the STXM chamber filled with He. Transmitted X-rays were measured as a function of the sample position (synchronized by an interferometer) to obtain X-ray images by optical density contrast. Image resolution was determined by the 25 nm zone plate and position steps. Elemental maps and NEXAFS spectra were obtained using image sequence scans over different photon energy ranges (520 eV to 600 eV for O K-edge) using the STAKS procedure implemented in the aXis2000 software.[59] Spectra at particular regions of interest in the sample were selected (regions allowing enough transmitted photons to be detected and excluding regions for which the optical density was too high to be in the Beer−Lambert's law linear regime). The images extracted from the "stack", which is a collection of images recorded at different photon energies close to the absorption edge, were then normalized with a virtual incident beam intensity measured through sample-free regions of the Si_3N_4 windows.

MEASUREMENTS OF CeO_2: Cerium dioxide was acquired from Alfa Aesar and prepared as a sintered pellet for measurements. The O K-edge XANES was recorded at beamline 7.0.1 of the Advanced Light Source (ALS)[60] of Lawrence Berkeley National Laboratory in total electron yield (TEY) mode. The monochromator resolution was about 0.3 eV.

The O K-edge of CeO_2 measured with NIXS was acquired at the ID20 beamline of the ESRF, Grenoble. Photons from three U26 undulators were monochromatized by a high-heat-load Si(111) monochromator and a successive Si(311) channel-cut monochromator and focused to a spot size

of 20 x 20 μm^2 at the sample position using a Kirkpatrick-Baez mirror system. The large solid angle spectrometer[61] was used and 36 out of 72 spherically bent Si(660) crystal analyzers recorded inelastically scattered photons with energy losses in the vicinity of the O K-edge. O K-edges were measured at momentum transfers of 3.5 $Å^{-1}$ and 9.5 $Å^{-1}$. The overall energy resolution was 0.7 eV. All data were extracted and treated as described in [42].

THEORETICAL CALCULATIONS. O K-edge XANES were calculated with the FDMNES[62–65] and FEFF9[66,67] codes and very good agreement with the experimental data was obtained from both codes. Because FDMNES allows analysis of the different components of the projected densities of states (DOS) and provides crystal orbital overlap populations (COOP),[68] only FDMNES results are reported in the main text while FEFF9 results are shown in the Supplementary Information (SI) for completeness. FDMNES is a self-consistent *ab initio* code based on the local-density approximation (LDA) DFT to calculate spectra related to the X-ray absorption process. It accounts for relativistic and spin-orbit effects and the presence of a core-hole. It implements two methods for calculations, the multiple-scattering theory (MS) and the finite difference methods (FDM). All calculations shown here were obtained with the FDM, which gives more precise results for the near-edge region. The potential was calculated self-consistently within a radius of 7 Å around the absorber and the same radius was used for the FDM calculations. Projected DOS are calculated with the atomic sphere approximation together with the XANES spectra. We additionally calculated the COOP. Relativistic and spin-orbit effects were included. The parameters for the convolution step were kept at the default value of the code. Only the core-hole lifetime was increased to 0.5 eV from 0.3 eV[69] to have better agreement for the width of the first sharp peak. To test the effect of the core-hole on the spectral shape, we ran calculations with and without the core-hole. We found only slight changes induced by the core-hole and we therefore

report calculations obtained with a non-excited absorber. The negligible effect of the core-hole derives probably by the dominance of Th DOS in the peaks at the O K absorption edge, as will be explained in the results and discussion section. To evaluate the effect of lattice expansion, the lattice constant was increased from 5.6032 Å to 5.6632 Å. To evaluate the effect of size reduction, the atomic coordinates of a spherical nanoparticle of 2.1 nm diameter were isolated from a ThO_2 slab. The spectra of the non-equivalent O atoms in the nanoparticle were obtained within a single calculation run to have the calculated spectra aligned to a common Fermi energy.

RESULTS AND DISCUSSION. ThO_2 and CeO_2 crystallize in the fluorite structure, with O surrounded by 4 metal ions in T_d local coordination and the metal ion surrounded by 8 O ions in cubic symmetry, i.e. arranged at the corner of the cube centered on the metal ion. In a cubic crystal field the *d* orbitals splits into a double-degenerate e_g and a triple-degenerate t_{2g} manifold, with the eg states at lower energy than the t2g states. The order is reversed compared to an octahedral crystal field, where the 6 ligands are along the axial directions.[70] A schematic of the splitting from cubic and octahedral crystal fields is shown in Figure S1. Figure 1 reports experimental data and calculation results for ThO_2 (panel a) and CeO_2 (panel b). The O K-edge XANES of ThO_2 was obtained in transmission mode from STXM. The two spectra of CeO_2 are from XANES collected in the TEY mode and a NIXS measurement. Theoretical calculations of spectra, projected DOS and COOP obtained with the FDMNES code are reported below the experimental data. The energy scale of experimental data is reported on the top axis while the bottom axis refers to the Fermi energy of calculations.

The O K-edge of both ThO_2 and CeO_2 are characterized by three prominent features, with the former having an additional weak feature riding on the low-energy side of the second prominent

peak. For ThO_2 the first peak is extremely sharp and intense; the middle peak is weaker and more structured with the low-energy small feature; and the third is intense and broad. For CeO_2, NIXS and XANES measurements are similar and characterized by two sharp peaks and a broader third one. The agreement between the calculated XANES with the experimental spectral shapes is very good for both systems, with relative intensities and energy positions of the peaks well reproduced. Despite the similarities of the two spectra, the interpretation of peaks is different resulting from the differences in the relative ordering and energy spread of the *f* and *d* orbitals, as revealed by inspection of the projected DOS and COOP.

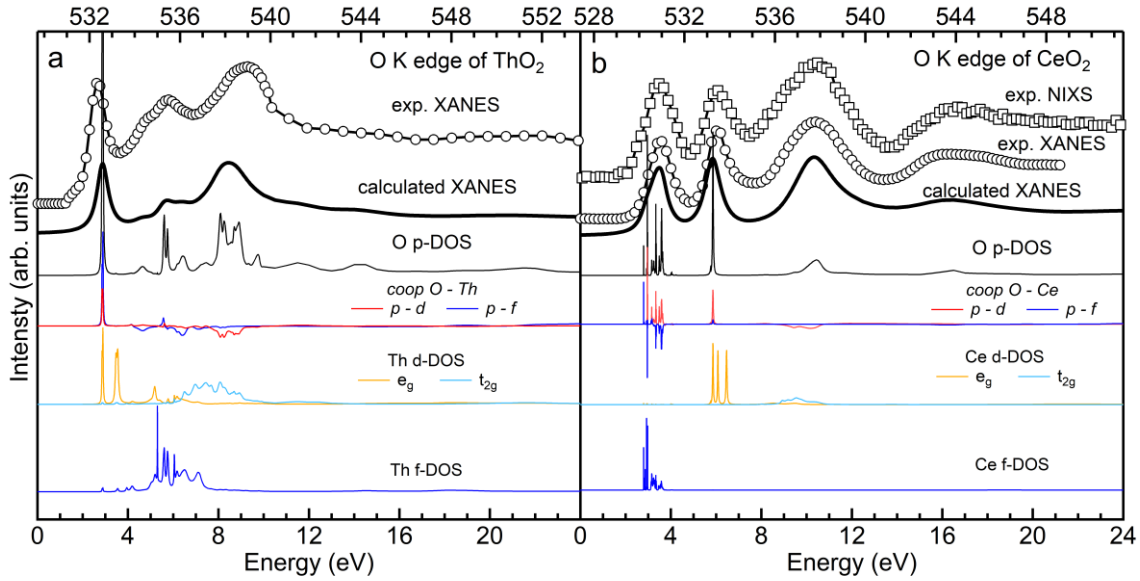

Figure 1. Experimental data (empty dots/squares) and O K-edge spectra calculated with FDMNES (thick black lines) of ThO_2 (panel a) and CeO_2 (panel b). For ThO_2, the experimental spectrum is a XANES obtained in transmission mode from STXM. For CeO_2, two spectra are shown, one obtained with NIXS (empty squares) and a XANES acquired in total electron yield (TEY). For both panels, below the calculated spectrum, the following results are reported: the O p DOS (black thin line); the COOP between O p and Th/Ce d and f orbitals (red thin line and blue thin line,

respectively); the e_g (yellow thin line) and t_{2g} (light-blue thin line) components of Th/Ce d-DOS; and the Th/Ce f-DOS (blue thin line).

As expected, all features of the calculated spectrum strongly correspond to structures found in the calculated O *p* DOS, which is shown below the simulated spectra in Figure 1. For a more detailed figure and labeling of the results, see Figure S2 in the Supplementary Information (SI). A first indication of which Th (Ce) orbitals contribute to the O K-edge spectrum is given by the position of the projected 5*f* (4*f*) and 6*d* (5*d*) bands of Th (Ce) with respect to the features of the O *p* DOS. In Figure 1 the metal *f*-DOS is shown in blue and the *d*-DOS is reported as the sum of the e_g-t_{2g} components (yellow and light-blue, respectively), resulting from the cubic crystal field (see Fig. S1). The ThO_2 5*f* DOS forms a broader band than that from the 4*f* DOS of CeO_2. This follows from the larger radial extent of the 5*f* allowing their participation in chemical bonds, and are found correspondingly in the middle peak of the O K-edge spectrum. Contrasting to this behavior, the sharper 4*f* band of CeO_2 corresponds to the first sharp peak in the O K-edge spectrum. In both systems, the *d*-DOS splits into e_g and t_{2g} components in a similar manner. The e_g band is the sum of two identical contributions from the d_{z2} and the d_{x2-z2} components and the t_{2g} band is the sum of three identical contributions from d_{xz}, d_{yz} and d_{xy}. The e_g band is composed of three sharp peaks at the low energy side of the broad t_{2g} band, reflecting the stronger hybridization of the t_{2g} with the O ligands from to the spatial orientation of the lobes, which gives stronger superposition with the O orbitals. The main difference between the ThO_2 and CeO_2 spectra are the larger separation of the e_g peaks in ThO_2. Comparison with the O *p* DOS reveals that in ThO_2 the first peak of the e_g DOS corresponds to the first very sharp peak of the O *p* DOS. Similarly, in CeO_2 the same e_g peak is found to correspond to the second sharp peak of the O *p* DOS. The broad

t_{2g} band corresponds to the third broad feature of the O p DOS in both systems. Assignment of the peaks can be finalized by inspection of the hybridization as given by the COOP, also shown in Figure 1. The positive, negative and null COOP correspond to bonding, antibonding and non-bonding interactions, respectively. Inspection of the p – d COOP (red) indicates bonding character for the first sharp e_g peak, non-bonding interaction with the other e_g peaks and antibonding character for the broad t_{2g} band in both CeO_2 and ThO_2, with the distinction that the hybridization with the e_g component of the d-DOS yields the first peak in ThO_2 spectrum and the second peak in the CeO_2 spectrum. The antibonding interaction with the t_{2g} band gives rise to the third peak of the XANES spectra in both systems. Inspection of the *p* – *f* COOP (blue) reveals a predominant antibonding interaction corresponding to the *f*-DOS of both systems, from which the middle and first XANES peak in ThO_2 and CeO_2 originate, respectively. A *p* – *f* bonding interaction is also present in corresponding to the e_g contribution, where the *f*-DOS is absent or very weak. This weak contribution may be due to the limits of the local-density approximation (LDA) DFT in treating localized orbitals like the *f*. The tendency is to overestimate their delocalization and as consequence their mixing with other orbitals.

The interpretation of the O K-edge XANES spectra of CeO_2 emerging from our calculations is in agreement with previous works[50,71,72] and the recent review by Frati et al.,[69] while the interpretation of ThO_2 O K-edge spectra based on spectral calculations is given here for the first time. The hybridization of O *p* orbitals with both Th (Ce) 6*d* (5*d*) and 5*f* (4*f*) orbitals makes the O K-edge a unique probe of the metal electronic structure, where all the orbitals relevant to the bonding are probed in a single energy regime without the perturbation of a core-hole localized on the metal center. Our calculations indicate that the O K-edge XANES of CeO_2 and ThO_2 reflect the ordering of *f* and *d* states expected for lanthanides and actinides.[53,54] In CeO_2 and in all

lanthanide dioxides, the 4*f* orbitals are lower than the 5*d* and form sharp bands due to the strong localization and weak interaction of the 4*f*. Differently, the ThO_2 5*f* states are predicted to be slightly higher than the 6*d* states.[53] The energy of the 5*f* states progressively decreases along the actinide series, with the crossover at PaO_2, making ThO_2 the only actinide dioxide with 5*f* orbitals higher than 6*d*. Indeed, this ordering is confirmed by the O K-edge spectra of UO_2, NpO_2, and PuO_2 where the contribution of the 5*f* states is at the absorption edge, just before the peak of the An 6*d*-e_g contribution.[36]

The stronger involvement of Th 5*f* orbitals in chemical bonding compared to Ce 4*f* is also clearly visible in the experimental O K-edge XANES spectra. The peak corresponding to the 4*f* orbitals of CeO_2 (first) is sharper than that due to the 5*f* orbitals of ThO_2 (middle). The projected *f*-DOS indicate that the Ce 4*f* forms a much sharper band than the Th 5*f*, because of the larger delocalization of the latter. These assignments are compatible with FEFF[67] calculations, reported in Figures S3 – S4 of the SI.

Lastly, the O *p* DOS hybridize with only part of the metal d DOS of e_g and t_{2g} nature as indicated by comparison of the DOS shapes. For the e_g contribution, this is clearly seen as only one peak of the e_g band appears in the O *p* DOS. Correspondingly in the t_{2g}, the *p* DOS has a contribution only at the higher energy part of the band. These details can be better observed in Figure S2.

Through the O K-edge XANES, the metal *d* and *f* contribution to chemical bonds can be probed at once and in the absence of a core-hole localized on the metal ion. The O K-edge is therefore expected to be quite sensitive to structural modifications. Theoretical calculations can help in rationalizing how spectral features react to structural changes and guide the interpretation of data on complex systems. With this scope, we investigated the effects of lattice expansion and size

reduction on ThO_2 by theoretical calculations. We focused on ThO_2 because of the stronger overlap of Th 5*f* and O 2*p*.

A variation of the lattice parameter is very frequently encountered in mixed metal oxide materials. In mixed actinide oxides, the lattice parameter varies linearly between that of the two end members[73] according to Vegard's Law while in ThO_2 nanoparticles of 2 nm size a 1% lattice expansion was recently reported.[74,75] Lattice variations are easily identified with X-ray diffraction (XRD). However, since XRD measures an average property of the system, the uniform variation of the lattice parameter does not correctly describe the local arrangement, as often evidenced when XRD and the results from extended X-ray absorption fine structure spectroscopy (EXAFS) are compared.[73] It is therefore interesting to see how the O K-edge XANES would be modified by lattice alterations. Figure 2 shows the calculated O K-edge XANES spectra for ThO_2 and for ThO_2 with 1% lattice expansion applied, corresponding to that observed for small nanoparticles.[74] The spectra have been aligned to the post-edge features, thus only relative energy positions are meaningful and comparable. The calculations predict that the three prominent peaks towards the edge threshold in the 1% expanded ThO_2 spectrum will get closer in energy. In particular, the third peak appears less affected since the relative distance from the post-edge features and the shape remain almost the same. On the other hand, the first and middle peaks get closer to each other. The first peak decreases significantly in intensity while the middle peak acquires intensity and sharpness. This behavior is consistent with the expected reaction of the electronic structure to a lattice expansion. The $e_g - t_{2g}$ splitting of 6*d* orbitals will decrease due to the weakening of the crystal field. For the same reasons, the width of the 5*f* band manifold is reduced from the decreased interaction with ligand orbitals. This behavior is reflected in the reduced energy separation of the first and third peaks and in the sharpening of the middle peak. The corresponding DOS are reported

in Figure S5 in SI. This is the scenario expected in case of a uniform expansion like the one described by the virtual crystal approximation. However, in the presence of pronounced local distortions, a broadening of spectral features is anticipated due to the presence of absorbers with different local configurations, which will yield different spectra.

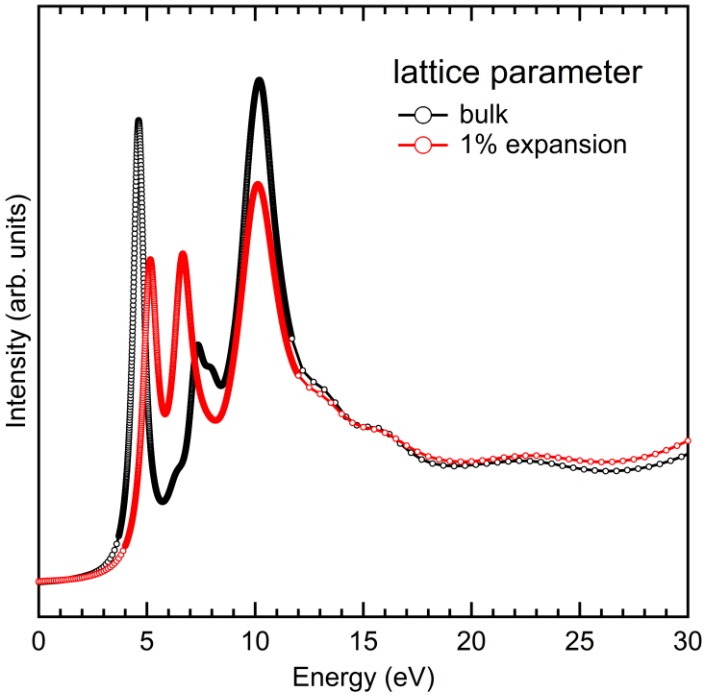

Figure 2. Calculated O K-edge XANES spectra for ThO_2 (black empty dots) and ThO_2 with a 1% lattice expansion (red empty dots) obtained with FDMNES.

The latter scenario can be partially considered by analyzing a nanoparticle, where the surface breaks the symmetry of the bulk creating a set of non-equivalent O absorbers. We considered a 2.1 nm spherical nanoparticle of ThO_2 and, in analogy with our previous work on ThO_2 nanoparticles at the Th L_3 edge,[76] we simulated the O K-edge XANES spectrum of the non-equivalent O absorbers. The nanoparticle structure was isolated from a chunk of bulk ThO_2. Surface reorganization and interaction with surfactants were neglected. The results reflect effects of the

surface and the reduced size as the consequences of symmetry break and lack of scatterers for a portion of absorbers. The results are shown in Figure 3, where 10 calculated spectra corresponding to the 10 non-equivalent O atoms in the nanoparticle are compared. The nanoparticle structure is shown in the inset together with absorbers near the surface identified. The local environment of all O atoms in the nanoparticle is schematically shown in Figure S6 of the SI. Absorbers 1 through 4 are inside the nanoparticle (first and second coordination shells as in bulk ThO_2); 5 and 6 are subsurface O atoms (second coordination shell different from bulk ThO_2); and 7 through 10 are surface atoms (first coordination shell different from bulk ThO_2). The three peaks characteristic of the O K-edge XANES spectra from bulk ThO_2 are well-distinguished for absorbers 1 through 6. Starting from the surface atoms, i.e. absorber 7, the first sharp peak is lost and the spectrum shows only two broad structures. The XANES spectra for all non-equivalent absorbers were obtained from a single calculation in order to have the spectra aligned to a common Fermi level. Because errors in the calculated Fermi energy of up to 1 eV are common in codes like FDMNES, the relative alignments have to be considered as qualitative. For absorbers 10 and 8, some low-energy peaks are observed well-below the main absorption edge. They appear because the calculated Fermi level is inside the occupied DOS. Both DOS and Fermi level are not accurately calculated because of the poor description of the structure at surface. Overall, the calculated spectra in Figure 3 indicate that O K-edge XANES spectra are very sensitive to changes in local coordination.

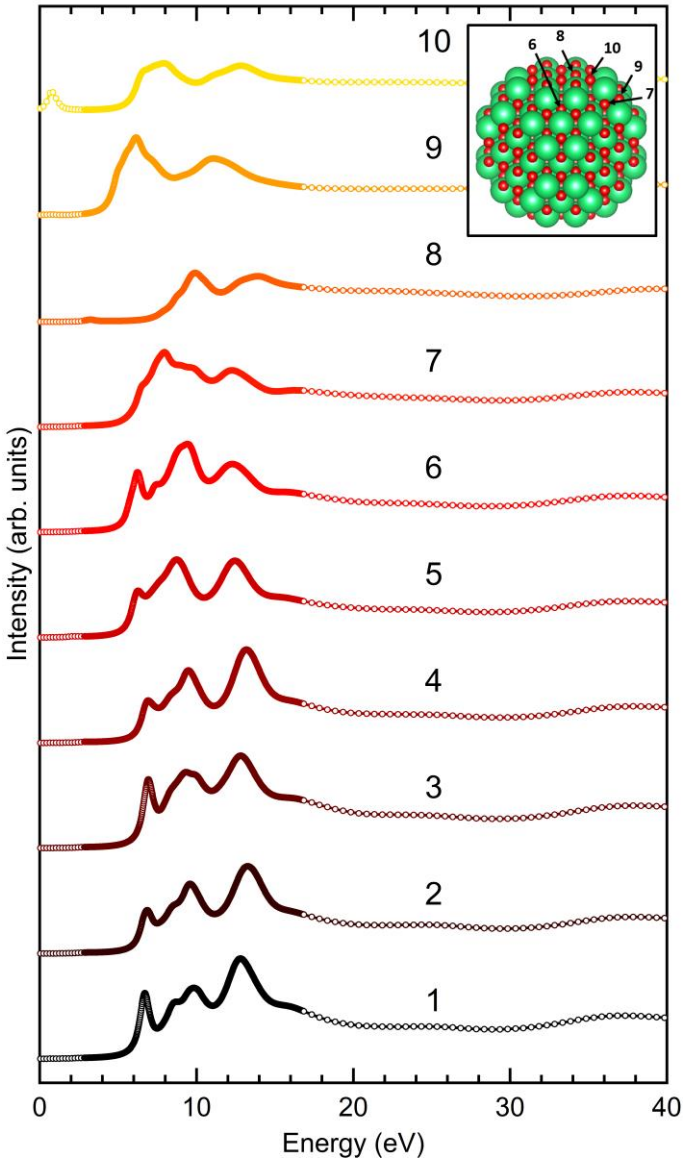

Figure 3. O K-edge XANES calculated with FDMNES for the 10 non-equivalent absorbers from a 2.1 nm nanoparticle of ThO_2. The nanoparticle structure and the O absorbers close to the surface are shown in the inset.

The O K-edge XANES spectra obtained by the weighted average of the non-equivalent absorbers is shown in Figure 4 together with the calculated XANES of bulk ThO_2 and of the oxygen at the center of the nanoparticle. The spectrum of the nanoparticle exhibits a much less intense first peak with broader features. As suggested by Figure 3, this is due to the contribution of surface atoms,

which represent 43% of all O atoms of the nanoparticle. This result is in agreement with the O K-edge data on ThO_2 nanoparticles embedded in a covalent organic framework by Moreau et al.,[51] where the first sharp peak observed on bulk ThO_2 is not present on the spectrum of NPs.

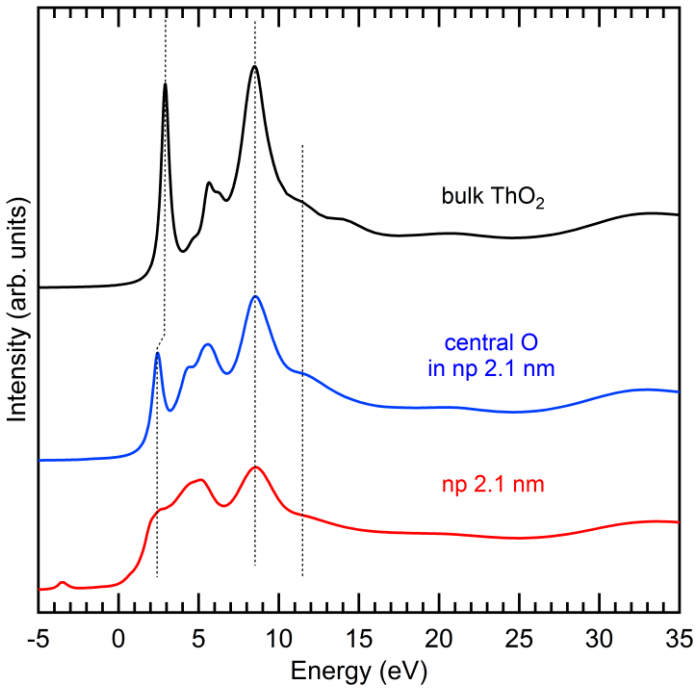

Figure 4. O K-edge XANES calculated with FDMNES for bulk ThO_2 (black), the central O atom of the 2.1 nm nanoparticle (blue) and the weighted average of all O absorber in the nanoparticle (red).

As expected, calculations predict a high sensitivity of O K-edge XANES spectral features to structural changes of ThO_2. Real systems can be characterized by complex structural changes, with the simultaneous presence of local distortions, changes of local coordination and of the lattice parameter. It is therefore desirable to construct a structural model as close as possible to the real system to extract information from O K-edge XANES spectra with the help of calculations especially in the cases of reduced dimensionality.

CONCLUSIONS.

The O K-edge XANES spectra of ThO_2 and CeO_2 are presented and interpreted based on DFT spectral calculations and inspection of the electronic structure. Spectral features derived from metal *d* and *f* states are clearly visible and form well-separated peaks, a direct proof of their hybridization with O orbitals. In CeO_2 the 4*f* band appears below the 5*d*, while in ThO_2 the 5*f* band is found between the 6*d* e_g and t_{2g} states, in agreement with the expected ordering of 5*f* and 6*d* orbitals in actinide dioxides. Comparison with the O K-edge spectra of CeO_2 and other early actinide dioxides confirms the assignment of spectral features and agrees with the predicted electronic structure of these systems.

Calculated O K-edge XANES for a 1% expansion of the lattice parameter and for a ThO_2 spherical nanoparticle of 2.1 nm diameter indicate a high sensitivity to structural changes. The change in local coordination of surface atoms gives more drastic spectral change and results in strong broadening and lowering of intensities from the main spectral features.

The insight given by O K-edge XANES spectra on the electronic structure of both ligand and metal is very promising for the study of lanthanide and actinide systems. The possibility to measure the O K-edge XANES spectrum with NIXS, which employs hard X-rays, is important for the actinide field as it avoids some difficulties that accompany and make soft X-ray XANES as well as electron-energy loss spectroscopy (EELS) complicated. Thus, NIXS presents a very promising avenue and means to measure O K-edge NIXS spectra on actinide compounds.

ASSOCIATED CONTENT

Supporting Information. Additional calculations performed with FEFF, scheme of the local environment of each O atom in the 2.1 nm nanoparticle. (PDF)

AUTHOR INFORMATION

Corresponding Author

*lucia.amidani@esrf.fr; kristina.kvashnina@esrf.fr

Author Contributions

The manuscript was written through contributions of all authors. All authors have given approval to the final version of the manuscript.

ORCID

Lucia Amidani 0000-0003-2234-4173

Thomas Dumas 0000-0001-6425-6484

David K. Shuh 0000-0002-3104-3260

Sergei M. Butorin 0000-0003-3242-5305

Christop J. Sahle 0000-0001-8645-3163

Alessandro Longo 0000-0002-8819-2128

Krisitna O. Kvashnina 0000-0003-4447-4542

Notes

Any additional relevant notes should be placed here.

ACKNOWLEDGMENT

L. A. acknowledges Yves Joly for useful discussions. We acknowledge support from the European Research Council (ERC) under grant agreement No. 759696. This work was supported in part by the U.S. Department of Energy (DOE), Director, Office of Science, Office of Basic Energy Sciences, Division of Chemical Sciences, Geosciences, and Biosciences Heavy Element

Chemistry Program under Contract No. DE-AC02-05CH11231 at LBNL (DKS). This research used resources of the Advanced Light Source, a U.S. DOE Office of Science User Facility under contract no. DE-AC02-05CH11231. S.M.B acknowledges the support from the Swedish Research Council (research grant 2017-06465).

REFERENCES

(1) Gibson, J. K.; de Jong, W. A. *Experimental and Theoretical Approaches to Actinide Chemistry*; Wiley, 2018.

(2) Liddle, S. T. The Renaissance of Non-Aqueous Uranium Chemistry. *Angew. Chem. Int. Ed.* **2015**, *54* (30), 8604–8641.

(3) Clark, D. L.; Hobart, D. E. Discovery of the Transuranium Elements Inspired Rearrangement of the Periodic Table and the Approach for Finding New Elements; Structure and Bonding; Springer Berlin Heidelberg: Berlin, Heidelberg, 2019.

(4) Prodan, I. D.; Scuseria, G. E.; Martin, R. L. Covalency in the Actinide Dioxides: Systematic Study of the Electronic Properties Using Screened Hybrid Density Functional Theory. *Phys. Rev. B* **2007**, *76* (3), 033101.

(5) Moore, K. T.; van der Laan, G. Nature of the 5f States in Actinide Metals. *Rev. Mod. Phys.* **2009**, *81* (1), 235–298.

(6) Neidig, M. L.; Clark, D. L.; Martin, R. L. Covalency in F-Element Complexes. *Coordination Chemistry Reviews* **2013**, *257* (2), 394–406.

(7) Lu, E.; Sajjad, S.; Berryman, V. E. J.; Wooles, A. J.; Kaltsoyannis, N.; Liddle, S. T. Emergence of the Structure-Directing Role of f-Orbital Overlap-Driven Covalency. *Nat Commun* **2019**, *10* (1), 634.

(8) Denning, R. G. Electronic Structure and Bonding in Actinyl Ions and Their Analogs. *J. Phys. Chem. A* **2007**, *111* (20), 4125–4143.

(9) Kerridge, A. Quantification of F-Element Covalency through Analysis of the Electron Density: Insights from Simulation. *Chem. Commun.* **2017**, *53* (50), 6685–6695.

(10) Pace, K. A.; Klepov, V. V.; Berseneva, A. A.; Loye, H. Covalency in Actinide Compounds. *Chem. Eur. J.* **2021**, *27* (19), 5835–5841.

(11) Kozimor, S. A.; Yang, P.; Batista, E. R.; Boland, K. S.; Burns, C. J.; Clark, D. L.; Conradson, S. D.; Martin, R. L.; Wilkerson, M. P.; Wolfsberg, L. E. Trends in Covalency for D- and f-Element Metallocene Dichlorides Identified Using Chlorine K-Edge X-Ray Absorption Spectroscopy and Time-Dependent Density Functional Theory. *J. Am. Chem. Soc.* **2009**, *131* (34), 12125–12136.

(12) Minasian, S. G.; Keith, J. M.; Batista, E. R.; Boland, K. S.; Clark, D. L.; Conradson, S. D.; Kozimor, S. A.; Martin, R. L.; Schwarz, D. E.; Shuh, D. K.; et al. Determining Relative f and d Orbital Contributions to M–Cl Covalency in MCl_6^{2-} (M = Ti, Zr, Hf, U) and $UOCl_5^-$ Using Cl K-Edge X-Ray Absorption Spectroscopy and Time-Dependent Density Functional Theory. *J. Am. Chem. Soc.* **2012**, *134* (12), 5586–5597.

(13) Su, J.; Batista, E. R.; Boland, K. S.; Bone, S. E.; Bradley, J. A.; Cary, S. K.; Clark, D. L.; Conradson, S. D.; Ditter, A. S.; Kaltsoyannis, N.; et al. Energy-Degeneracy-Driven Covalency in Actinide Bonding. *J. Am. Chem. Soc.* **2018**, *140* (51), 17977–17984.

(14) Minasian, S. G.; Keith, J. M.; Batista, E. R.; Boland, K. S.; Bradley, J. A.; Daly, S. R.; Kozimor, S. A.; Lukens, W. W.; Martin, R. L.; Nordlund, D.; et al. Covalency in Metal–Oxygen Multiple Bonds Evaluated Using Oxygen K-Edge Spectroscopy and Electronic Structure Theory. *J. Am. Chem. Soc.* **2013**, *135* (5), 1864–1871.

(15) Sergentu, D.-C.; Autschbach, J. Covalency in Actinide(IV) Hexachlorides in Relation to the Chlorine K-Edge X-Ray Absorption Structure. *Chem. Sci.* **2022**, *13* (11), 3194–3207.

(16) Lukens, W. W.; Speldrich, M.; Yang, P.; Duignan, T. J.; Autschbach, J.; Kögerler, P. The Roles of 4f- and 5f-Orbitals in Bonding: A Magnetochemical, Crystal Field, Density

Functional Theory, and Multi-Reference Wavefunction Study. *Dalton Trans.* **2016**, *45* (28), 11508–11521.
(17) Bagus, P. S.; Schacherl, B.; Vitova, T. Computational and Spectroscopic Tools for the Detection of Bond Covalency in Pu(IV) Materials. *Inorg. Chem.* **2021**, *60* (21), 16090–16102.
(18) Bagus, P. S. Covalent Interactions in Oxides. *Journal of Electron Spectroscopy and Related Phenomena* **2014**, 8.
(19) Kvashnina, K. O.; Butorin, S. M. High-Energy Resolution X-Ray Spectroscopy at Actinide M $_{4,5}$ and Ligand K Edges: What We Know, What We Want to Know, and What We Can Know. *Chem. Commun.* **2022**, *58* (3), 327–342.
(20) Kvashnina, K. O.; Butorin, S. M.; Martin, P.; Glatzel, P. Chemical State of Complex Uranium Oxides. *Phys. Rev. Lett.* **2013**, *111* (25), 253002.
(21) Kvashnina, K. O.; Romanchuk, A. Yu.; Pidchenko, I.; Amidani, L.; Gerber, E.; Trigub, A.; Rossberg, A.; Weiss, S.; Popa, K.; Walter, O.; et al. A Novel Metastable Pentavalent Plutonium Solid Phase on the Pathway from Aqueous Plutonium(VI) to PuO $_2$ Nanoparticles. *Angew. Chem. Int. Ed.* **2019**, *58* (49), 17558–17562.
(22) Leinders, G.; Bes, R.; Pakarinen, J.; Kvashnina, K.; Verwerft, M. Evolution of the Uranium Chemical State in Mixed-Valence Oxides. *Inorg. Chem.* **2017**, *56* (12), 6784–6787.
(23) Butorin, S. M.; Kvashnina, K. O.; Vegelius, J. R.; Meyer, D.; Shuh, D. K. High-Resolution X-Ray Absorption Spectroscopy as a Probe of Crystal-Field and Covalency Effects in Actinide Compounds. *Proceedings of the National Academy of Sciences* **2016**, *113* (29), 8093–8097.
(24) Vitova, T.; Green, J. C.; Denning, R. G.; Löble, M.; Kvashnina, K.; Kas, J. J.; Jorissen, K.; Rehr, J. J.; Malcherek, T.; Denecke, M. A. Polarization Dependent High Energy Resolution X-Ray Absorption Study of Dicesium Uranyl Tetrachloride. *Inorganic Chemistry* **2015**, *54* (1), 174–182.
(25) Butorin, S. M.; Kvashnina, K. O.; Smith, A. L.; Popa, K.; Martin, P. M. Crystal-Field and Covalency Effects in Uranates: An X-Ray Spectroscopic Study. *Chem. Eur. J.* **2016**, *22* (28), 9693–9698.
(26) Gerber, E.; Romanchuk, A. Yu.; Pidchenko, I.; Amidani, L.; Rossberg, A.; Hennig, C.; Vaughan, G. B. M.; Trigub, A.; Egorova, T.; Bauters, S.; et al. The Missing Pieces of the PuO_2 Nanoparticle Puzzle. *Nanoscale* **2020**, 17951–18480.
(27) Amidani, L.; Vaughan, G. B. M.; Plakhova, T. V.; Romanchuk, A. Yu.; Gerber, E.; Svetogorov, R.; Weiss, S.; Joly, Y.; Kalmykov, S. N.; Kvashnina, K. O. The Application of HEXS and HERFD XANES for Accurate Structural Characterisation of Actinide Nanomaterials: The Case of ThO $_2$. *Chem. Eur. J.* **2021**, *27* (1), 252–263.
(28) Amidani, L.; Retegan, M.; Volkova, A.; Popa, K.; Martin, P. M.; Kvashnina, K. O. Probing the Local Coordination of Hexavalent Uranium and the Splitting of 5f Orbitals Induced by Chemical Bonding. *Inorg. Chem.* **2021**, *60* (21), 16286–16293.
(29) Tobin, J. G.; Nowak, S.; Booth, C. H.; Bauer, E. D.; Yu, S.-W.; Alonso-Mori, R.; Kroll, T.; Nordlund, D.; Weng, T.-C.; Sokaras, D. Separate Measurement of the $5f_{5/2}$ and $5f_{7/2}$ Unoccupied Density of States of UO_2. *Journal of Electron Spectroscopy and Related Phenomena* **2019**, *232*, 100–104.
(30) Vitova, T.; Pidchenko, I.; Biswas, S.; Beridze, G.; Dunne, P. W.; Schild, D.; Wang, Z.; Kowalski, P. M.; Baker, R. J. Dehydration of the Uranyl Peroxide Studtite, [$UO_2(\eta^2$-

$O_2)(H_2O)_2]\cdot 2H_2O$, Affords a Drastic Change in the Electronic Structure: A Combined X-Ray Spectroscopic and Theoretical Analysis. *Inorg. Chem.* **2018**, *57* (4), 1735–1743.
(31) Hunault, M. O. J. Y.; Lelong, G.; Cormier, L.; Galoisy, L.; Solari, P.-L.; Calas, G. Speciation Change of Uranyl in Lithium Borate Glasses. *Inorg. Chem.* **2019**, *58* (10), 6858–6865.
(32) Hunault, M. O. J. Y.; Menut, D.; Tougait, O. Alkali Uranyl Borates: Bond Length, Equatorial Coordination and 5f States. *Crystals* **2021**, *11* (1), 56.
(33) Dalodière, E.; Virot, M.; Morosini, V.; Chave, T.; Dumas, T.; Hennig, C.; Wiss, T.; Dieste Blanco, O.; Shuh, D. K.; Tyliszcak, T.; et al. Insights into the Sonochemical Synthesis and Properties of Salt-Free Intrinsic Plutonium Colloids. *Sci Rep* **2017**, *7* (1), 43514.
(34) Spurgeon, S. R.; Sassi, M.; Ophus, C.; Stubbs, J. E.; Ilton, E. S.; Buck, E. C. Nanoscale Oxygen Defect Gradients in UO_{2+x} Surfaces. *Proc. Natl. Acad. Sci. U.S.A.* **2019**, *116* (35), 17181–17186.
(35) Modin, A.; Yun, Y.; Suzuki, M.-T.; Vegelius, J.; Werme, L.; Nordgren, J.; Oppeneer, P. M.; Butorin, S. M. Indication of Single-Crystal PuO_2 Oxidation from O 1s x-Ray Absorption Spectra. *Phys. Rev. B* **2011**, *83* (7), 075113.
(36) Modin, A.; Suzuki, M.-T.; Vegelius, J.; Yun, Y.; Shuh, D. K.; Werme, L.; Nordgren, J.; Oppeneer, P. M.; Butorin, S. M. 5*f*-Shell Correlation Effects in Dioxides of Light Actinides Studied by O 1*s* x-Ray Absorption and Emission Spectroscopies and First-Principles Calculations. *J. Phys.: Condens. Matter* **2015**, *27* (31), 315503.
(37) Dumas, T.; Guillaumont, D.; Fillaux, C.; Scheinost, A.; Moisy, P.; Petit, S.; Shuh, D. K.; Tyliszczak, T.; Auwer, C. D. The Nature of Chemical Bonding in Actinide and Lanthanide Ferrocyanides Determined by X-Ray Absorption Spectroscopy and Density Functional Theory. *Phys. Chem. Chem. Phys.* **2016**, *18* (4), 2887–2895.
(38) Dumas, T.; Guillaumont, D.; Moisy, P.; Shuh, D. K.; Tyliszczak, T.; Solari, P. L.; Den Auwer, C. The Electronic Structure of F-Element Prussian Blue Analogs Determined by Soft X-Ray Absorption Spectroscopy. *Chem. Commun.* **2018**, *54* (86), 12206–12209.
(39) Fillaux, C.; Guillaumont, D.; Berthet, J.-C.; Copping, R.; Shuh, D. K.; Tyliszczak, T.; Auwer, C. D. Investigating the Electronic Structure and Bonding in Uranyl Compounds by Combining NEXAFS Spectroscopy and Quantum Chemistry. *Phys. Chem. Chem. Phys.* **2010**, *12* (42), 14253.
(40) Solomon, E. I.; Hedman, B.; Hodgson, K. O.; Dey, A.; Szilagyi, R. K. Ligand K-Edge X-Ray Absorption Spectroscopy: Covalency of Ligand–Metal Bonds. *Coordination Chemistry Reviews* **2005**, *249* (1–2), 97–129.
(41) Schülke, W. *Electron Dynamics by Inelastic X-Ray Scattering*; Oxford Science Publications; Oxford University Press, 2007.
(42) Sahle, Ch. J.; Mirone, A.; Niskanen, J.; Inkinen, J.; Krisch, M.; Huotari, S. Planning, Performing and Analyzing X-Ray Raman Scattering Experiments. *J Synchrotron Rad* **2015**, *22* (2), 400–409.
(43) Caciuffo, R.; van der Laan, G.; Simonelli, L.; Vitova, T.; Mazzoli, C.; Denecke, M. A.; Lander, G. H. Uranium 5d − 5f Electric-Multipole Transitions Probed by Nonresonant Inelastic x-Ray Scattering. *Phys. Rev. B* **2010**, *81* (19), 195104.
(44) Sundermann, M.; van der Laan, G.; Severing, A.; Simonelli, L.; Lander, G. H.; Haverkort, M. W.; Caciuffo, R. Crystal-Field States of UO_2 Probed by Directional Dependence of Nonresonant Inelastic x-Ray Scattering. *Phys. Rev. B* **2018**, *98* (20), 205108.

(45) Sundermann, M.; Simonelli, L.; Huotari, S.; Eloirdi, R.; Lander, G. H.; Caciuffo, R.; van der Laan, G. Transuranium Compounds Probed by Nonresonant Inelastic X-Ray Scattering. *Phys. Rev. B* **2020**, *101* (7), 075103.
(46) Amorese, A.; Sundermann, M.; Leedahl, B.; Marino, A.; Takegami, D.; Gretarsson, H.; Gloskovskii, A.; Schlueter, C.; Haverkort, M. W.; Huang, Y.; et al. From Antiferromagnetic and Hidden Order to Pauli Paramagnetism in UM_2Si_2 Compounds with 5*f* Electron Duality. *Proc Natl Acad Sci USA* **2020**, *117* (48), 30220–30227.
(47) Mizuno, Y.; Ohmura, Y. Theory of X-Ray Raman Scattering. *J. Phys. Soc. Jpn.* **1967**, *22* (2), 445–449.
(48) Bradley, J. A.; Yang, P.; Batista, E. R.; Boland, K. S.; Burns, C. J.; Clark, D. L.; Conradson, S. D.; Kozimor, S. A.; Martin, R. L.; Seidler, G. T.; et al. Experimental and Theoretical Comparison of the O K-Edge Nonresonant Inelastic X-Ray Scattering and X-Ray Absorption Spectra of $NaReO_4$. *J. Am. Chem. Soc.* **2010**, *132* (39), 13914–13921.
(49) Löble, M. W.; Keith, J. M.; Altman, A. B.; Stieber, S. C. E.; Batista, E. R.; Boland, K. S.; Conradson, S. D.; Clark, D. L.; Lezama Pacheco, J.; Kozimor, S. A.; et al. Covalency in Lanthanides. An X-Ray Absorption Spectroscopy and Density Functional Theory Study of $LnCl_6^{x-}$(*x*=3, 2). *J. Am. Chem. Soc.* **2015**, *137* (7), 2506–2523.
(50) Minasian, S. G.; Batista, E. R.; Booth, C. H.; Clark, D. L.; Keith, J. M.; Kozimor, S. A.; Lukens, W. W.; Martin, R. L.; Shuh, D. K.; Stieber, S. C. E.; et al. Quantitative Evidence for Lanthanide-Oxygen Orbital Mixing in CeO_2, PrO_2, and TbO_2. *J. Am. Chem. Soc.* **2017**, *139* (49), 18052–18064.
(51) Moreau, L. M.; Herve, A.; Straub, M. D.; Russo, D. R.; Abergel, R. J.; Alayoglu, S.; Arnold, J.; Braun, A.; Deblonde, G. J. P.; Liu, Y.; et al. Structural Properties of Ultra-Small Thorium and Uranium Dioxide Nanoparticles Embedded in a Covalent Organic Framework. *Chem. Sci.* **2020**, 10.1039.C9SC06117G.
(52) Straub, M. D.; Ouellette, E. T.; Boreen, M. A.; Branson, J. A.; Ditter, A.; Kilcoyne, A. L. D.; Lohrey, T. D.; Marcus, M. A.; Paley, M.; Ramirez, J.; et al. Thorium Amidates Function as Single-Source Molecular Precursors for Thorium Dioxide. *Chem. Commun.* **2021**, *57* (40), 4954–4957.
(53) Wen, X.-D.; Martin, R. L.; Henderson, T. M.; Scuseria, G. E. Density Functional Theory Studies of the Electronic Structure of Solid State Actinide Oxides. *Chem. Rev.* **2013**, *113* (2), 1063–1096.
(54) Sevik, C.; Çağın, T. Mechanical and Electronic Properties of CeO_2, ThO_2, and $(Ce,Th)O_2$ Alloys. *Phys. Rev. B* **2009**, *80* (1), 014108.
(55) Grandjean, S.; Beres, A.; Rousselle, J.; Maillard, C. Procédé de Coprécipitation d'actinides à Des États d'oxydation Distincts et de Pré-Paration de Composés Mixtes d'actinides. WO 2005/119699.
(56) Arab-Chapelet, B.; Grandjean, S.; Nowogrocki, G.; Abraham, F. Synthesis of New Mixed Actinides Oxalates as Precursors of Actinides Oxide Solid Solutions. *Journal of Alloys and Compounds* **2007**, *444–445*, 387–390.
(57) Arab-Chapelet, B.; Grandjean, S.; Nowogrocki, G.; Abraham, F. Synthesis and Characterization of Mixed An(IV)An(III) Oxalates (An(IV)=Th, Np, U or Pu and An(III)=Pu or Am). *Journal of Nuclear Materials* **2008**, *373* (1–3), 259–268.
(58) Nilsson, H. J.; Tyliszczak, T.; Wilson, R. E.; Werme, L.; Shuh, D. K. Soft X-Ray Scanning Transmission X-Ray Microscopy (STXM) of Actinide Particles. *Anal Bioanal Chem* **2005**, *383* (1), 41–47.

(59) AXis2000 Is Written in Interactive Data Language (IDL). It Is Available Free for Non-Commercial Use from Http://Unicorn.Mcmaster.ca/AXis2000.Html.
(60) Warwick, T.; Heimann, P.; Mossessian, D.; McKinney, W.; Padmore, H. Performance of a High Resolution, High Flux Density SGM Undulator Beamline at the ALS (Invited). *Review of Scientific Instruments* **1995**, *66* (2), 2037–2040.
(61) Huotari, S.; Sahle, Ch. J.; Henriquet, Ch.; Al-Zein, A.; Martel, K.; Simonelli, L.; Verbeni, R.; Gonzalez, H.; Lagier, M.-C.; Ponchut, C.; et al. A Large-Solid-Angle X-Ray Raman Scattering Spectrometer at ID20 of the European Synchrotron Radiation Facility. *J Synchrotron Rad* **2017**, *24* (2), 521–530.
(62) Bunău, O.; Ramos, A. Y.; Joly, Y. The *FDMNES* Code. In *Volume I: X-ray absorption spectroscopy and related techniques*; International Tables for Crystallography; 2021.
(63) Joly, Y.; Cavallari, C.; Guda, S. A.; Sahle, C. J. Full-Potential Simulation of X-Ray Raman Scattering Spectroscopy. *J. Chem. Theory Comput.* **2017**, *13* (5), 2172–2177.
(64) Bunău, O.; Joly, Y. Self-Consistent Aspects of x-Ray Absorption Calculations. *J. Phys.: Condens. Matter* **2009**, *21* (34), 345501.
(65) Bunău, O.; Joly, Y. Time-Dependent Density Functional Theory Applied to x-Ray Absorption Spectroscopy. *Phys. Rev. B* **2012**, *85* (15), 155121.
(66) Kas, J. J.; Vila, F. D.; Rehr, J. J. The *FEFF* Code. In *Volume I: X-ray absorption spectroscopy and related techniques*; International Tables for Crystallography; 2020.
(67) Rehr, J. J.; Kas, J. J.; Vila, F. D.; Prange, M. P.; Jorissen, K. Parameter-Free Calculations of X-Ray Spectra with FEFF9. *Phys. Chem. Chem. Phys.* **2010**, *12* (21), 5503.
(68) Diaz-Lopez, M.; Guda, S. A.; Joly, Y. Crystal Orbital Overlap Population and X-Ray Absorption Spectroscopy. *J. Phys. Chem. A* **2020**, *124* (29), 6111–6118.
(69) Frati, F.; Hunault, M. O. J. Y.; de Groot, F. M. F. Oxygen K-Edge X-Ray Absorption Spectra. *Chem. Rev.* **2020**, *120* (9), 4056–4110.
(70) Burns, R. G. *Mineralogical Applications of Crystal Field Theory*, 2nd ed.; Cambridge Topics in Mineral Physics and Chemistry; Cambridge University Press, 1993.
(71) Garvie, L. A. J.; Buseck, P. R. Determination of Ce^{4+} /Ce^{3+} in Electron-Beam-Damaged CeO_2 by Electron Energy-Loss Spectroscopy. *Journal of Physics and Chemistry of Solids* **1999**, 5.
(72) Wu, Z. Y.; Jollet, F.; Gota, S.; Thromat, N.; Gautier-Soyer, M.; Petit, T. X-Ray Absorption at the Oxygen K Edge in Cubic f Oxides Examined Using a Full Multiple-Scattering Approach. *J. Phys.: Condens. Matter* **1999**, *11* (37), 7185–7194.
(73) Hubert, S.; Purans, J.; Heisbourg, G.; Moisy, P.; Dacheux, N. Local Structure of Actinide Dioxide Solid Solutions $Th_{1-x}U_xO_2$ and $Th_{1-x}Pu_xO_2$. *Inorg. Chem.* **2006**, *45* (10), 3887–3894.
(74) Plakhova, T. V.; Romanchuk, A. Yu.; Likhosherstova, D. V.; Baranchikov, A. E.; Dorovatovskii, P. V.; Svetogorov, R. D.; Shatalova, T. B.; Egorova, T. B.; Trigub, A. L.; Kvashnina, K. O.; et al. Size Effects in Nanocrystalline Thoria. *J. Phys. Chem. C* **2019**, *123* (37), 23167–23176.
(75) Plakhova, T. V.; Romanchuk, A. Yu.; Seregina, I. F.; Svetogorov, R. D.; Kozlov, D. A.; Teterin, Y. A.; Kuzenkova, A. S.; Egorov, A. V.; Kalmykov, S. N. From X-Ray Amorphous ThO_2 to Crystalline Nanoparticles through Long-Term Aging at Room Temperature. *J. Phys. Chem. C* **2023**, *127* (1), 187–195.
(76) Amidani, L.; Plakhova, T. V.; Romanchuk, A. Yu.; Gerber, E.; Weiss, S.; Efimenko, A.; Sahle, C. J.; Butorin, S. M.; Kalmykov, S. N.; Kvashnina, K. O. Understanding the Size Effects on the Electronic Structure of ThO_2 Nanoparticles. *Phys. Chem. Chem. Phys.* **2019**, *21* (20), 10635–10643.

BRIEFS (Word Style “BH_Briefs”). If you are submitting your paper to a journal that requires a brief, provide a one-sentence synopsis for inclusion in the Table of Contents.

SYNOPSIS (Word Style “SN_Synopsis_TOC”). If you are submitting your paper to a journal that requires a synopsis, see the journal’s Instructions for Authors for details.